Toward direct, micron-scale XRF elemental maps and quantitative profiles of wet marine sediments

Philipp Böning, Edouard Bard, and Jérôme Rose
CEREGE – Collège de France, UMR6635 CNRS, University Paul Cézanne Aix-Marseille III, Europôle de l'Arbois, BP80, F-13545 Aix-en-Provence Cedex 4, France (philipp@cerege.fr)

[1] Here we describe a chemical analysis technique for Ca, Fe, K, Sr, Ti, and S using a recently developed Micro-XRF analyzer (Micro-XRF) with a 100-μm resolution and an XRF whole-core scanner (XRF-S) with a 5-mm resolution for selected sediment sections from a continental margin sediment core. The Micro-XRF produces highly resolved element maps of individual sections, and the calculation of individual continuous element profiles is based on overlap measurements of successive sections. By means of discrete subsamples analyzed by ICP-OES, the two XRF data sets are successfully calibrated to provide quantitative profiles of Ca, Fe, K, Sr, and Ti. We discuss the advantages and limitations of both XRF techniques. A comparison of the two independent XRF data sets demonstrates the overall high consistency and accuracy of both techniques. The resulting element profiles and detailed XRF maps clearly show that the Micro-XRF is a powerful tool for studying at high resolution the chemical transitions linked to paleoenvironmental changes. For example, the discrimination between provenance changes and diagenetical effects on the Fe profile can be achieved by the combined inspection of the Fe/Ti profile and S maps. This highlights the usefulness of the XRF maps for clarification of profile ambiguities and clearly distinguishes the Micro-XRF from other technical devices producing elemental profiles only.

1. Introduction

[2] Over the last few years, significant progress has been made in the field of high-resolution analysis of natural samples based on X-ray imaging techniques (micro-absorption, micro-fluorescence, transmission and tomography). Micro X-Ray Fluorescence Analysis (Micro-XRF) is one of the techniques that has been developed very rapidly, mainly by means of synchrotron radiation and X-ray focusing devices. Since it is non-destructive and able to map samples on a micrometer (μm) scale, Micro-XRF is nowadays a well-established analytical method over a wide range of fields of application, such as materials science, archaeometry, life sciences and, as shown here, geochemical studies.

[3] High-resolution studies on continuous sedimentary archives are much in demand for the understanding of high-frequency climate change on a seasonal to millennial scale. Consequently, it

is necessary to look at individual chemical and structural phase transitions in closer detail, which offers the possibility of linking geochemistry, sedimentology and mineralogy in combined studies. This important issue can be addressed using Micro-XRF, whose resolution is better than the millimeter scale.

[4] We present data on calcium (Ca), iron (Fe), strontium (Sr), potassium (K) and titanium (Ti), which are important constituents of marine sediments commonly used as tracers for paleoenvironmental reconstructions. Biogenic Ca and Sr typically indicate the presence of calcareous organisms (made of calcite or aragonite), whereas the other elements usually indicate the presence of lithogenic material or diagenetical sulphides (Fe). Elemental XRF scanners, with a resolution of several mm, are commonly used to detect these and other elements in sediments from various ancient and recent marine environments [e.g., *Peterson et al.*, 2000; *Röhl and Abrams*, 2000]. By contrast, only few published XRF data are available for wet marine sediments on a sub-millimeter scale [*von Rad et al.*, 2002; *Haug et al.*, 2003; *Kido et al.*, 2006].

[5] In this paper, we present (1) a technique using the XGT 5000 Micro-XRF analyzer recently developed by Horiba-Jobin-Yvon, (2) elemental data (Ca, Fe, K, Sr and Ti) from partly laminated continental margin sediments acquired with Micro-XRF and a routinely used whole-core XRF Scanner (abbreviated here as XRF-S), (3) the successful calibration of both XRF data sets to element contents derived from ICP-OES, (4) a cross-check of both quantified Micro-XRF and XRF-S data, and (5) a promising outlook on the application of Micro-XRF to paleo-environmental studies.

2. Materials and Methods

2.1. Sample Selection Strategy

[6] The material for this study stems from core MD04-2876 (~25 m length) retrieved during cruise MD 143 CHAMAK of the Marion Dufresne in September/October 2004. The working half of the core was sampled with u-channels. The sediments of this specific core are made up of clays with varying amounts of $CaCO_3$ (min. 5 to max. 40 wt%). In the laboratory, the u-channels were analyzed using the Avaatech® XRF whole-core scanner. Then, 67 samples were taken from the entire core for chemical analysis by ICP-OES. For the subsequent Micro-XRF analysis (XGT 5000

Horiba Jobin-Yvon), we selected two independent sections (40 cm each), one from the upper and one from the lower half of the core. The first section represents a transition from dark, laminated and carbonate-bearing to light, non-laminated and carbonate-rich sediments (called *Section 1*), whereas the second section represents dark laminated and carbonate-bearing sediments with varying degrees of lamination preservation (called *Section 2*). A total of 39 samples were taken from both sections for Micro-XRF data calibration. For further technical details, see below.

2.2. XRF Core Scanner

[7] The XRF-S (Avaatech® XRF whole-core scanner at the University of Bremen) is a non-destructive routine analysis system for scanning the surface of sediment cores or u-channels [*Jansen et al.*, 1998; *Röhl and Abrams*, 2000]. The XRF-S is equipped with a Molybdenum X-ray source (3–50 kV), a Si(Li) Peltier-cooled PSI energy-dispersive X-ray (EDX) spectrometer (Kevex™) with a 125-μm beryllium window and a multichannel analyzer. This system configuration allows the analysis of elements from Al (atomic no. 13) to Ba (atomic no. 56).

[8] Prior to daily analysis, the instrument was calibrated against a set of pressed powder standards [*Jansen et al.*, 1998]. The sediment surface was lightly scraped with a microscope slide (parallel to lamination) to obtain a clean, smooth and flat surface. After that, the sediment surface was covered with Ultralene® X-ray transmission foil to avoid desiccation. Over the entire core, we analyzed statistically significant element intensities of Ca, Fe, K and Ti at 0.5-cm intervals, each measurement covering an area of 0.4 cm² (0.4 cm long × 1 cm wide), using a 30-s count time, 10 kV X-ray voltage and a current of 0.6 mA. The X-ray spot size was obtained using lateral slits. Acquired XRF spectra were processed with the Kevex™ software Toolbox© (including successive application of background subtraction, sum-peak and escape-peak correction, deconvolution and peak integration [*Röhl and Abrams*, 2000]). The resulting data are expressed as element intensities in counts per second (cps). Heterogeneities due to variable water content, porosity, grain-size differences and rough surfaces lead to scattering and bias in the scanner data which is commonly of the order of ~200 cps at the 2000 cps level [*Jansen et al.*, 1998].

2.3. Micro XRF Analyzer

[9] The XGT-5000 X-ray Analysis Microscope (Horiba-Jobin-Yvon), here referred to as Micro-
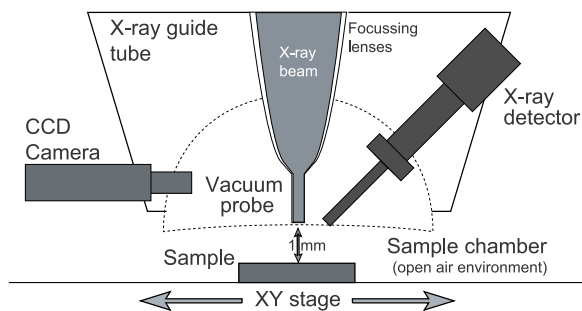
Figure 1. Schematic view of the measuring chamber of the XGT-5000 Micro-XRF Analyzer (Horiba−Jobin-Yvon) at CEREGE. The incident beam hits the sample surface perpendicularly, while the detector makes an angle of 45° with the sample surface. Image not to scale.

XRF, was designed to measure and analyze simultaneously the X-ray spectrum, the transmitted X-ray image and the fluorescent X-ray image (or map) of a sample. The Micro-XRF is a non-destructive analysis system for high-resolution scanning of hard or soft sample surfaces [e.g., *Rose et al.*, 2006]. The highly focused and intense X-ray beam is generated with a Rhodium X-ray tube (15−50 kV) using a current adjustable up to 1 mA and focused with X-ray guide tubes, whose inner diameter is either 100 or 10 μm (Figure 1) [*Hosokawa et al.*, 1997]. X-ray emission from the irradiated sample is detected with an energy-dispersive X-ray (EDX) spectrometer equipped with a liquid-nitrogen-cooled high-purity Si detector. The system configuration allows the analysis of elements from Na (atomic no. 11) to U (atomic no. 92). An X-ray

tube voltage of 50 kV is applied with a current of 1.0 mA and an X-ray radiation diameter of 100 μm for the determination of Ca, Fe, K, Sr and Ti by using their Kα line intensities.

[10] The analysis probe chamber of the XGT-5000 (X-ray source and detector) is under vacuum (Figure 1), which increases sensitivity for light elements. However, samples are analyzed under the probe in the xy direction at normal atmospheric pressure. A constant distance of 1 mm is maintained between the analysis probe chamber and the sediment surface to minimize absorption effects by the air between the probe and the sample.

[11] Prior to analysis, the u-channels in the studied core were carefully cut into 20 cm segments to fit the relatively small analysis chamber (Figure 2). Care was taken not to loose or squeeze out sediment at the margins of each segment, so as to avoid disturbing the sedimentary continuity. The sediment surface was covered with a PVC thin film (Ecopla®, 10 μm thick) to avoid desiccation. Each segment was stored in a gas-tight plastic box and kept cool at 4°C.

[12] First, an element map of 5.12 × 5.12 cm (26.2 cm^2) was produced covering two segments (called the *reference overlap*; shown as a green rectangle on the left in Figure 2). Then, for each segment, a map of 5.12 cm x 1.28 cm (6.55 cm^2) was constructed, which overlapped the *reference* by a length of about 1.2 cm and a maximum width of 1.28 cm (∼1.54 cm^2). Consequently, further maps of 6.55 cm^2 were produced that overlapped each other by ∼1.54 cm^2.
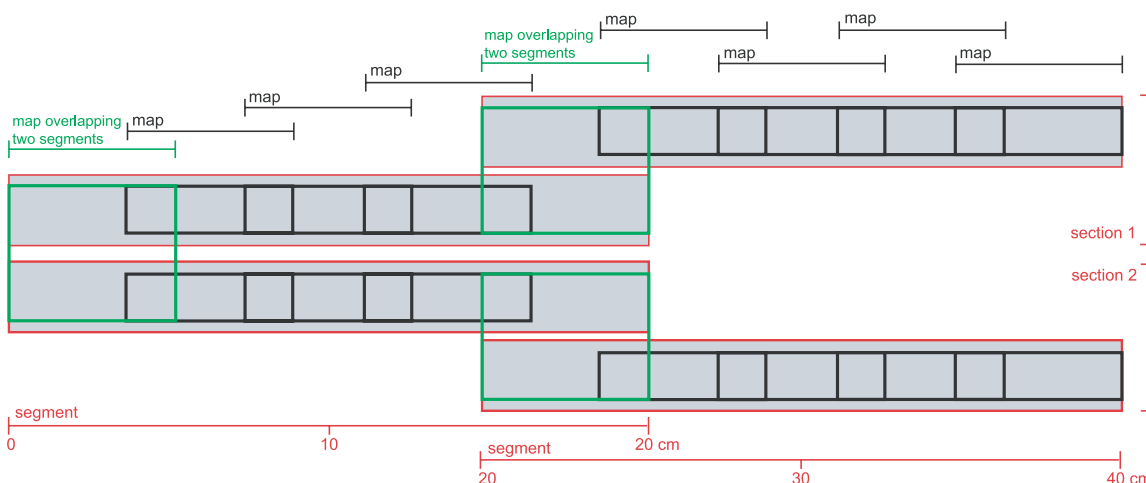

Figure 2. Diagram showing the measuring protocol of the Micro-XRF on the two 40 cm sediment sections.

a)

b)

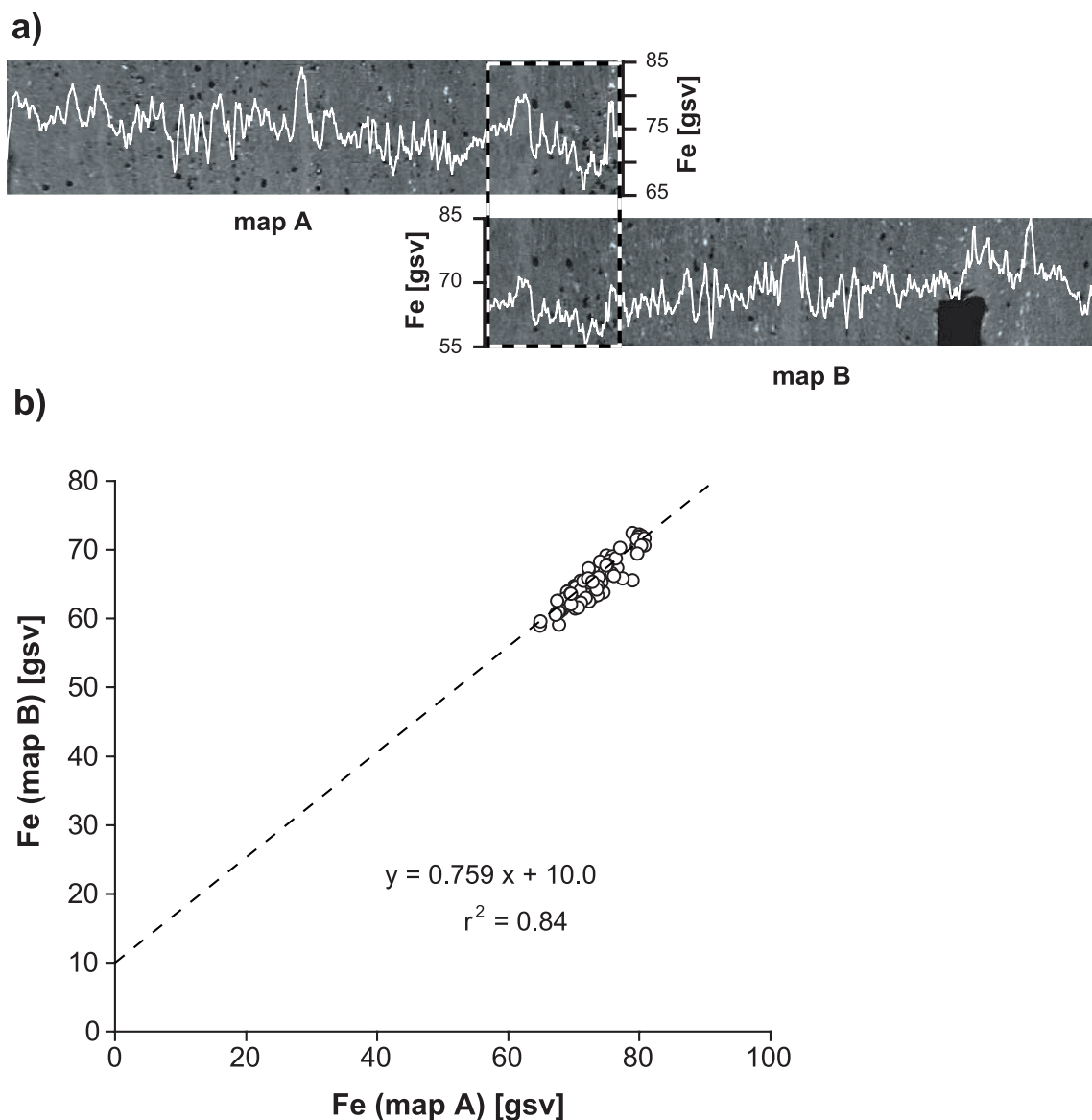$$y = 0.759\ x + 10.0$$

$$r^2 = 0.84$$

Figure 3. Example of the data processing described in the text. (a) Two successive maps with corresponding elemental profiles. The area of the overlap is indicated by the dashed rectangle. (b) Scatterplot of the data from the two overlapping maps: gsv, grayscale values.

[13] For optimum counting, the measuring time was 15 ms per pixel (i.e., 0.1 × 0.1 mm, i.e., one data point) repeated at least 25 times resulting in a measuring time of ~7 h per 6.55 cm². For each pixel in the XRF map the software first deconvolved the measured XRF spectrum to element counts, which were then auto-converted to grayscale values using a linear interpolation. Each data point along the downcore profile (along the x axis) is the average value of a maximum of 128 pixels (map width or y direction) resulting in element profiles with 512 data points (map length or x direction). For each point on the x axis representing 100 μm, the counting time was therefore at least 34 s. Obvious cracks and holes were discarded for element profile calculation.

[14] To obtain an element profile for the entire segment of 20 cm, the individual profiles had to be fitted to the profile from the reference overlap. This resulted in scatterplots with a linear regression (according to the equation y = $a \bullet$ x + b). For elements such as Fe, Ca, and Sr, the squared correlation coefficient r^2 is high and significant, ranging between 0.72 and 0.95 (a representative
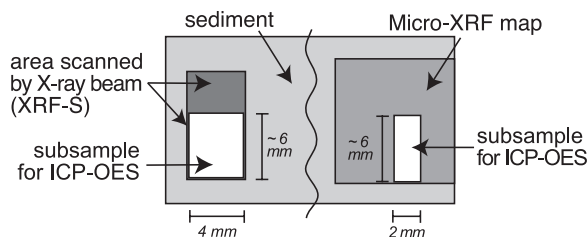
Figure 4. Sketch showing subsamples taken for the quantification of XRF-S and Micro-XRF data using ICP-OES.

segment is shown in Figures 3a and 3b). The linear equation was then used to rescale the profiles and element maps in order to make them fully compatible. In effect, the slope a and intercept b allow us to correct for slight changes of the sensitivity and baseline between different scans of the Micro-XRF instrument.

[15] For K and Ti, however, a larger scatter was obtained for overlapping profiles, which resulted in smaller r^2 values ranging between 0.38 and 0.66. Consequently, the different profiles were just matched by adjusting their average values by adding (or subtracting) only a constant value. Admittedly, this simplified procedure is probably less satisfactory than the previous one because it only takes into account changes of the baseline.

2.4. Calibration Based on Chemical Analyses of Subsamples

[16] The subsamples taken for the quantification of the XRF-S and the Micro-XRF data sets were chosen to cover the whole range of element concentrations. Figure 4 shows a schematic example of a subsample taken for the calibration of the XRF-S and Micro-XRF. To make it possible to carry out subsequent Micro-XRF analyses, the width of discrete subsamples was only about half of the XRF-S beam area. Hence the sampling dimensions were about $4 \times 6 \times 10$ mm for XRF-S subsamples and $2 \times 6 \times 5$ mm for Micro-XRF subsamples. The solid-phase subsamples were stored in polyethylene bags or cups, freeze-dried and homogenized in an agate mortar. The water contents were determined for the Micro-XRF subsamples and found to be in the range of $31.3 \pm 4.5\%$.

[17] Total contents of Ti, Fe, Ca, K and Sr were determined using routine ICP-OES (Perkin Elmer 3000 XL) after digestion in closed PTFE vessels performed according to *Heinrichs and Herrmann* [1990]. The samples (50 mg) were treated with

1 mL concentrated HNO_3 overnight to oxidize organic matter and dissolve carbonates. After that, 3 mL conc. HF and 1 mL conc. $HClO_4$ were added, and the vessels were heated for 12 h at 180°C. HNO_3 and $HClO_4$ were purified by subboiling distillation, while HF was of suprapure quality. After digestion, acids were evaporated on a heated metal block (180°C), residues were redissolved and fumed off three times with 3 mL 6N HCl, followed by redissolution with 1 mL conc. HNO_3 and subsequent dilution to 50 mL.

[18] Due to the (necessarily) low sample amount used in this study (50 mg), the digesting performance was tested by duplicate and triplicate sample digests of geostandards and sediment samples covering the entire concentration range where applicable. When there was enough sample powder, ten sediment samples covering the whole concentration range were additionally fused to glass beads and analyzed using conventional XRF spectrometry (Philips PW 2400) according to the routine method described by *Schnetger et al.* [2000]. Overall analytical precision and accuracy (see Table 1) were tested by (1) replicate digestion and analysis of geostandards GSD-12, PACS-1, GSR-6, several in-house standards and sediment samples and (2) comparison of ICP-OES and conventional XRF spectrometry data.

2.5. Potential Limitations Using XRF Techniques

[19] The potential limitations of both Micro-XRF and XRF-S are linked to small-scale heterogeneities due to variable porosity, water content, grain-size differences as well as matrix effects (absorption/enhancement) [e.g., *Tertian and Claisse*, 1982]. These latter effects may occur when part of the emitted fluorescence of Fe and Ti is absorbed or scattered by increasing Ca contents, whereas part of the fluorescence emitted by Ca may additionally excite K.

Table 1. Overall Precision and Accuracy for Analyzed Elements[a]

	Precision (1σ), %	Accuracy (1σ), %
Ca	1.9	2.6
Fe	2.2	3.7
Ti	2.7	2.4
K	2.4	4.4
Sr	2.9	2.7

[a] ICP-OES and conventional XRF spectrometry.

[20] However, the larger scatter observed for Ti Micro-XRF data (section 2.3) is linked rather to the extremely heterogeneous distribution of minute separate Ti phases as can be seen on the distribution maps (for example, see Figure 8). The larger scatter for K data can be explained by the fact that the detection of K (the lightest element analyzed) could be influenced by a variety of absorption effects (see the recent work by *Kido et al.* [2006]). Alternatively, it could be affected by the quality of the film covering the sediment surface: preliminary results based on the element maps showed that total XRF transmission of K was reduced by about 20% when using the PVC thin film compared with Mylar X-ray transmission film. In other words, the element map of K was about 20% darker when using PVC thin film. However, no differences were found for Ca. By contrast, for Ti, Fe and Sr, the Mylar film even reduced the total transmission by 20–25% compared with the PVC film. These findings are rather surprising since Mylar film normally does not affect the transmission of elements with an X-ray energy yield > 4 keV. Since the total attenuation of the Ti signal would have been too high with Mylar film, combined with the other limitations cited above, we hence decided to use the PVC film for our analyses.

[21] Quantitative analyses are typically made more difficult by matrix effects, the interstitial water content and the thin water film formed between the sediment surface and the thin film, especially for light elements such as Al, Si (and K). *Kido et al.* [2006] recently proposed a correction of these effects by a variety of experiments and calculations. These authors present a quantification of Al, Si, K, Ca, Ti and Fe by analyzing the cumulative XRF spectra of these elements [*Koshikawa et al.*, 2003] using a similar Micro-XRF (XGT 2700) over intervaled areas of 2.5 cm diameter and comparing their results with those obtained from conventional XRF spectrometry. The samples were selected from two different fine-grained wet marine sediments with a slightly higher range of element concentrations and higher water contents (the latter ranging from 36 to 65%) compared to our study. They estimated the absorption effects caused by the thin film and the thin water film (significant only for Al and Si), as well as the interstitial water and the matrix (effect of Ca on Fe, K and Ti), by analyzing the selected samples in their original wet state and after drying. A principal finding (and important for our study) is that the detection of K with the Micro-XRF is greatly hampered when water contents increase. Even if the water content

of the sediments in our study is ≤35%, we should still expect a certain effect of the interstitial water on the detection of K. Otherwise, it should be noted that our study is based on the use of XRF element maps (and not the incrementally stepped XRF scans), since it is important to maintain a 100-μm resolution for the structural and mineralogical information contained in the element maps.

3. Results and Discussion

[22] All data discussed here are presented in Tables 2 and 3. It is important to note that we compare data from two different techniques: (1) chemical data (Micro-XRF and XRF-S) obtained from a wet, microscopically uneven and physically/chemically heterogeneous upper layer of sediment of the order of tens to hundreds of microns thick, scanned by the X-ray beam, and (2) chemical data (ICP-OES) obtained from dried and homogenized sediment samples that were then completely dissolved. Therefore the absolute size of the volume scanned by XRF is associated with a certain error due to typical heterogeneity effects. Hence it is quite natural to expect a certain degree of data scatter rather than a perfect correlation between XRF and ICP-OES data.

3.1. Micro-XRF

[23] As mentioned above (section 2.3) and shown in Figures 2 and 3, we adjusted single measurements (element maps and profiles) to the reference overlap map and profile in order to obtain consistent and accurate element profiles for the two sections. To facilitate the comparison between Micro-XRF and ICP-OES data, it was necessary to average the signal over the Micro-XRF map corresponding to the area subsampled for the chemical analysis (see Figure 4). This Micro-XRF average value was then plotted against its corresponding ICP-OES data point (Figure 5).

[24] For all elements, we observe an excellent correlation between the Micro-XRF and ICP-OES data ($r^2 \geq 0.97$), except for K ($r^2 = 0.89$). The value of the intercept is also relatively high for K and Sr. In general, the element concentration range is larger for *Section 1* than for *Section 2*. As shown in Figures 5a and 5e, Sr exhibits the largest concentration range (with no concentration overlap between the two sections), while K exhibits the smallest range. Except for Sr, we obtain higher correlation coefficients for the elements from *Section 1* than for those from *Section 2* due to

Table 2. Data for Sr, Ca, Fe, K, and Ti Measured With ICP-OES, Micro-XRF, and XRF-S for the Two Sections of Core MD042876[a]

Depth, cm	ICP-OES					Micro-XRF					XRF-S			
	Sr, ppm	Ca, %	Fe, %	K, %	Ti, %	Sr, cgsv	Ca, cgsv	Fe, cgsv	K, cgsv	Ti, cgsv	Ca, cps	Fe, cps	K, cps	Ti, cps
695.70	712	8.05	3.67	1.96	0.341	87.2	22.1	42.7	26.3	11.3	*31277*	*25503*	*6239*	*2145*
696.85	934	9.74	3.21	1.87	0.330	94.6	21.8	40.6	25.1	10.8	*37943*	*21270*	*5235*	1820
699.65	1090	9.53	3.61	1.89	0.329	103	24.1	41.9	25.4	10.6	*37583*	*21796*	*5602*	1750
700.80	1374	9.81	3.35	1.96	0.327	125	25.4	38.7	25.2	10.3	37393	21886	5861	1845
701.90	570	6.01	4.12	2.29	0.398	76.8	16.7	52.3	29.3	13.4	43410	19448	5288	1625
702.95	1800	11.8	2.97	1.68	0.301	148	29.2	36.6	24.7	10.0	43031	18239	5077	1571
704.40	1642	10.7	3.13	1.86	0.324	118	22.3	40.8	24.0	10.7	47721	16838	4737	1453
705.80	1957	12.6	2.75	1.55	0.282	162	28.2	32.7	20.8	8.79	*48631*	*16378*	*4260*	*1269*
706.85	860	7.20	3.76	2.15	0.373	77.1	17.6	46.8	23.6	11.4	48486	16425	4524	1273
708.35	2158	12.8	2.66	1.54	0.286	172	30.0	31.8	20.2	8.68	*51201*	*14819*	*3928*	*1184*
710.75	2142	12.9	2.50	1.46	0.274	206	33.4	30.2	20.0	8.42	52557	13854	3806	1171
711.65	2002	12.6	2.85	1.47	0.272	163	29.2	33.9	20.8	9.06	*48154*	*16315*	*4216*	*1262*
712.60	2055	12.8	2.54	1.49	0.281	178	30.4	31.7	19.5	8.39	51283	15054	3784	1246
713.95	2046	12.7	2.53	1.48	0.280	167	29.0	30.3	19.0	8.41	52636	14147	3904	1179
716.75	2353	14.4	2.54	1.50	0.265	188	34.2	29.7	20.5	8.22	*52133*	*14388*	*3713*	*1204*
719.30	2611	15.4	2.25	1.46	0.259	201	37.5	26.8	20.1	7.69	*54229*	*13410*	*3810*	*1191*
721.30	2089	14.4	2.37	1.46	0.260	188	35.7	30.7	19.5	8.41	*53567*	*12790*	*3823*	*1110*
723.75	1770	13.1	2.61	1.57	0.285	167	27.6	30.9	19.7	8.62	*51177*	*14612*	*3942*	*1171*
724.85	1815	12.2	3.11	1.66	0.295	150	27.2	35.8	20.7	8.46	51927	14662	4058	1203
725.75	1722	12.5	*(3.31)*	1.53	0.282	164	29.1	*(32.8)*	20.6	8.09	*49664*	*15408*	*4008*	*1324*
728.15	2077	13.4	2.46	1.48	0.272	182	31.1	29.6	20.9	8.59	51553	13844	3737	1276
731.20	2127	13.4	2.53	1.53	0.269	178	31.9	30.4	20.6	8.37	*51860*	*13861*	*3707*	*1154*
733.60	2144	13.5	2.56	1.52	0.272	183	32.9	30.8	20.2	8.19	52927	14351	3988	1346
1932.30	226	5.93	3.74	2.06	0.406	50.8	13.0	47.9	25.2	12.8	*25142*	*25215*	*6384*	*2357*
1933.55	237	6.09	3.67	2.01	0.397	51.5	13.5	48.7	25.5	13.3	25247	27274	6942	2319
1935.15	229	6.13	3.64	2.11	0.403	51.3	13.2	48.4	25.2	12.6	25532	26732	6577	2331
1936.55	216	5.85	3.90	2.16	0.420	49.8	13.8	51.4	26.5	13.9	21142	28797	6986	2583
1937.55	222	5.99	3.85	2.08	0.404	49.3	12.2	49.6	25.8	13.5	24023	27257	6884	2367
1938.75	238	6.35	3.80	2.10	*(0.467)*	50.4	13.5	49.1	25.9	*(13.4)*	*24036*	*27982*	*7022*	*2380*
1946.80	260	6.70	3.78	2.11	0.397	52.8	16.2	49.5	27.8	13.4	28072	25669	6439	2229
1948.80	261	6.44	3.90	2.17	0.417	52.0	15.9	51.2	28.1	13.7	*27294*	*26941*	*6983*	*2400*
1950.75	216	5.50	3.82	2.18	0.384	48.9	11.6	50.2	28.4	12.9	*27251*	*26372*	*6373*	*2195*
1952.50	184	4.98	4.01	2.21	0.394	47.7	11.4	50.4	27.2	12.5	27336	25444	6725	2255
1954.20	198	5.11	3.80	2.27	0.399	46.6	10.4	48.9	27.7	12.7	*26394*	*25601*	*6259*	*2234*
1956.55	116	3.65	4.04	2.31	0.427	43.5	9.5	54.7	29.4	14.2	23457	27823	7135	2456
1958.65	190	5.09	4.37	1.98	0.374	47.9	11.0	54.8	24.9	11.6	24219	28575	7073	2351
1960.55	218	5.79	4.03	2.07	0.370	50.8	12.9	52.3	24.5	11.8	26196	26557	6689	2296
1962.90	263	*(6.32)*	3.66	1.93	0.356	52.4	*(10.9)*	46.0	24.5	11.6	27459	24922	6464	2228
1965.70	131	4.13	4.03	*(2.33)*	0.415	44.7	10.6	53.1	*(24.3)*	12.8	*29699*	*24305*	*6518*	*2088*

[a] Micro-XRF is the average from 20 data points, given in corrected grayscale values (cgsv). XRF-S is in counts per second (cps). Note that some of the values of the XRF-S (given in italics) are interpolated to fit the depth of ICP-OES and Micro-XRF samples. Four data couples in parentheses/ italics were excluded from the correlation (Figure 3) according to the following reasons: In the case of Fe (Ca), sediment became distinctly darker (lighter) with increasing sampling depth adding a portion of pyrite (carbonate) to the subsample, which was formerly not detected by the XRF beam (which as aforementioned only penetrates the upper 1 mm). In the case of Ti and K we assume a similar sample heterogeneity effect explaining the data inconsistency; however, since Ti and K do not contribute to the sediment color so visibly like Fe and Ca do, this remains unclear. Nevertheless, if these four individual fliers were included in the correlation, the effect on the correlation equation would be completely negligible.

their wider concentration ranges. Except for Ca (Figure 5d), which exhibits a negligible y axis intercept, we observe slightly positive intercepts for Sr and K as well as slightly negative intercepts for Ti and Fe. There is an absence of very low values for Ti, K and Fe (Figures 5b, 5c, and 5e), so the relationship between Micro-XRF and ICP-OES

data is not well defined at very low contents, which may also influence the intercept for these three elements. Furthermore, it is clear that the lowest values of K and Ti show the strongest scatter (Figures 5b and 5e), which could also influence the gradient and intercept of the regression line. (Note that very low contents of Fe, Ti and K are not

Table 3. Ca, Fe, K, and Ti Measured With ICP-OES and XRF-S for the Entire Core MD042876

Depth, cm	Ca, %	Fe, %	K, %	Ti, %	Ca, cps	Fe, cps	K, cps	Ti, cps
145.0	4.99	4.41	2.11	0.420	20132	29070	6371	2275
170.0	5.34	4.30	2.07	0.407	20351	29023	6446	2508
198.5	4.49	4.57	2.07	0.410	17528	28110	6031	2167
217.5	4.22	4.64	2.26	0.441	18771	30784	7092	2523
245.5	4.33	4.16	2.49	0.490	19882	30874	7160	2579
249.5	4.44	4.33	2.09	0.418	20159	29164	6880	2438
254.5	4.74	4.51	2.17	0.415	21321	28332	6759	2442
304.5	4.42	4.53	2.23	0.424	19282	31948	6832	2756
340.0	4.57	4.33	2.14	0.428	19154	30606	7020	2598
350.5	4.87	4.53	2.37	0.437	19575	30251	7019	2585
372.0	4.56	4.66	2.26	0.430	18230	32802	6769	2532
400.0	4.79	4.58	2.32	0.441	17992	31390	7579	2669
440.5	5.61	4.52	2.32	0.430	20367	29259	6951	2530
445.0	5.84	4.36	2.27	0.421	22237	28508	6865	2377
462.0	6.27	4.27	2.20	0.410	24293	28644	6867	2322
470.0	5.57	4.40	2.24	0.428	22731	29016	6916	2578
490.0	5.19	4.59	2.34	0.435	21285	30202	6909	2611
520.0	5.07	4.70	2.37	0.429	21367	30302	7454	2528
542.5	4.06	4.83	2.44	0.463	18456	32404	7906	2730
570.0	6.36	4.56	2.12	0.404	25471	27413	6741	2396
585.0	8.54	3.52	1.80	0.360	34522	21923	5521	1916
592.0	7.63	3.64	1.87	0.379	33453	23917	5965	2013
601.5	7.63	3.71	1.88	0.382	31637	24446	6066	2169
635.0	5.90	4.28	2.22	0.425	24463	29333	6979	2329
656.0	6.18	4.46	2.16	0.408	24941	29647	7068	2432
730.0	12.6	2.73	1.45	0.303	53870	13264	3778	1237
740.5	13.1	2.73	1.44	0.306	51648	14375	3916	1319
770.0	12.6	2.75	1.43	0.297	51995	14669	4069	1368
805.0	10.4	2.94	1.59	0.329	45696	17711	4608	1477
845.0	8.11	3.43	1.73	0.358	35923	22410	5820	2040
870.0	6.63	3.50	1.71	0.355	30514	24211	6243	2036
901.5	7.20	3.67	1.88	0.382	28898	24834	6016	2187
915.0	6.98	3.56	1.85	0.379	31185	23939	6297	2241
929.0	4.38	4.32	2.28	0.441	18146	27666	6689	2549
950.5	6.83	3.65	1.94	0.393	28224	25470	6354	2339
1006.5	4.81	4.23	2.24	0.452	22740	28193	7781	2539
1094.0	8.32	3.40	1.82	0.374	32915	21283	5716	2066
1161.0	8.80	3.21	1.80	0.368	38017	18269	5171	1778
1197.5	10.2	3.05	1.75	0.358	42962	17035	4736	1856
1201.5	8.92	3.34	1.70	0.357	37235	19270	5316	1876
1229.0	6.68	3.58	1.96	0.398	25637	25986	6588	2335
1250.0	8.06	3.55	1.80	0.374	33711	21851	5870	2118
1311.0	4.18	4.28	2.01	0.421	17706	31321	6579	2661
1340.5	6.97	3.42	1.83	0.377	29917	24042	6079	2173
1414.0	10.8	2.93	1.68	0.349	42683	17671	4963	1630
1450.5	7.91	3.69	1.94	0.393	29798	25124	6321	2119
1526.0	10.4	2.87	1.73	0.356	42674	17573	4854	1763
1576.5	6.17	3.84	2.18	0.427	24532	27711	7068	2367
1627.0	4.42	4.29	2.49	0.479	19776	31756	7937	2652
1723.5	7.44	3.70	1.95	0.403	29757	24442	6062	2229
1732.0	6.73	3.96	2.05	0.409	28443	27551	6083	2110
1770.0	8.41	3.17	1.79	0.376	37634	20846	5719	2071
1814.0	6.41	4.33	2.00	0.382	26519	26938	6601	2328
1842.0	4.04	4.83	2.56	0.473	19309	30681	8303	2759
1899.5	6.36	3.64	2.01	0.403	27426	25112	6301	2299
1940.5	3.74	4.72	2.52	0.467	18953	30992	8197	2772
1957.5	5.77	4.13	2.26	0.436	22116	29699	7559	2600
2018.5	9.10	3.24	1.83	0.370	36300	20847	5537	1960
2041.5	8.22	3.41	1.88	0.384	34423	21938	5905	1941
2101.0	6.83	3.56	1.93	0.391	30807	23922	6564	2310
2120.0	6.82	3.58	1.90	0.384	29887	24376	6512	2262
2129.5	6.43	3.79	2.17	0.426	27688	26122	6757	2254

Table 3. (continued)

Depth, cm	Ca, %	Fe, %	K, %	Ti, %	Ca, cps	Fe, cps	K, cps	Ti, cps
2199.5	6.81	3.57	2.02	0.409	28383	25608	6364	2357
2260.5	4.64	3.46	2.48	0.483	22026	27912	7110	2700
2339.5	6.59	4.29	1.96	0.396	25175	27700	7093	2635
2421.5	3.74	4.34	2.34	0.476	15825	32741	8106	2871
2502.5	7.21	3.38	1.99	0.405	32319	21471	6110	2187

likely to occur in the remainder of the sediment core since the concentration range for these elements is fully covered by the two sections presented here). A further reason for the non-zero intercepts might be related to the matrix effects of Ca on Fe, Ti and K [*Tertian and Claisse*, 1982]: part of the emitted fluorescence of Fe and Ti may be absorbed or scattered by increasing Ca contents, resulting in a negative intercept for Fe and Ti. By contrast, part of the emitted fluorescence of Ca may additionally excite K resulting in a positive intercept for K. Given all these influencing factors, it is difficult to account for the non-zero values of the intercepts, at least for K and Ti. By contrast, the positive intercept for Sr seems to be well defined, as indicated by the very good correlation coefficient for the very-low-content samples of *Section 2* and the small error on the intercept (Figure 5a). These features might be caused by the generally higher XRF background when using high voltage (50 kV). Nevertheless, the Micro-XRF is hence capable of detecting a quantifiable content of at least 130 ppm Sr (0.013 wt%).

[25] Absorption effects due to water content as well as matrix effects cannot be corrected since they are inherent to the map. As such, they must be put into relation to the averaging of highly heterogeneous areas for profile calculation.

[26] In any case, the very significant correlations observed between the Micro-XRF and ICP-OES data clearly show that all relationships are linear for the concentration range presented here. This is true not only for Ca, Fe and Sr, but also for Ti and K, even if matching between individual Micro-XRF maps is more difficult for the two latter elements (see section 2.3).

3.2. XRF-S

[27] For the quantification of the XRF-S data, we used two different data sets (Tables 2 and 3): the first consists of the data points distributed over the entire core and the second is obtained from both sections (ICP-OES subsamples taken originally for the Micro-XRF data acquisition, see 3.1). The depths (y axis) for the second data set do not always exactly match the depths of the XRF-S data points. Therefore the values for the XRF-S were partly interpolated (by 2.5 mm) to fit the exact depth of ICP-OES and Micro-XRF samples.

[28] From Figure 6, very good correlations ($r^2 \geq 0.87$) become apparent between chemical data and their correspondent scanner data. The two data sets show very little deviation from each other since they plot in the same area. For all elements, the total concentration range is slightly increased, further supporting the quality of the linear regressions. The second data set exhibits a rather low scatter, even if some data points are interpolated for depth and despite the fact that subsamples are only 2 mm thick, i.e., smaller than the 4 mm XRF-S beam (Figure 4).

[29] Similarly to the Micro-XRF data discussed above, we observe slightly negative intercepts for Fe, Ti and K (Figures 6a, 6c, and 6d), but a slightly positive intercept for Ca (Figure 6b). In the case of Fe, Ti and K, the lowest XRF-S values correspond to the highest Ca values and plot slightly below the respective regression lines. As already mentioned

Figure 5. Scatterplots for (a) Sr, (b) Ti, (c) Fe, (d) Ca, and (e) K obtained from Micro-XRF (in corrected grayscale values, cgsv) and ICP-OES (in % or ppm). In each legend the correlation coefficient is given for the individual sections. Dashed lines indicate the 95% confidence interval; dotted lines indicate the zero on the y axis. The regression equations are given in each graph, with corresponding deviations for the gradient and intercept. See also Table 2 and text for further details.
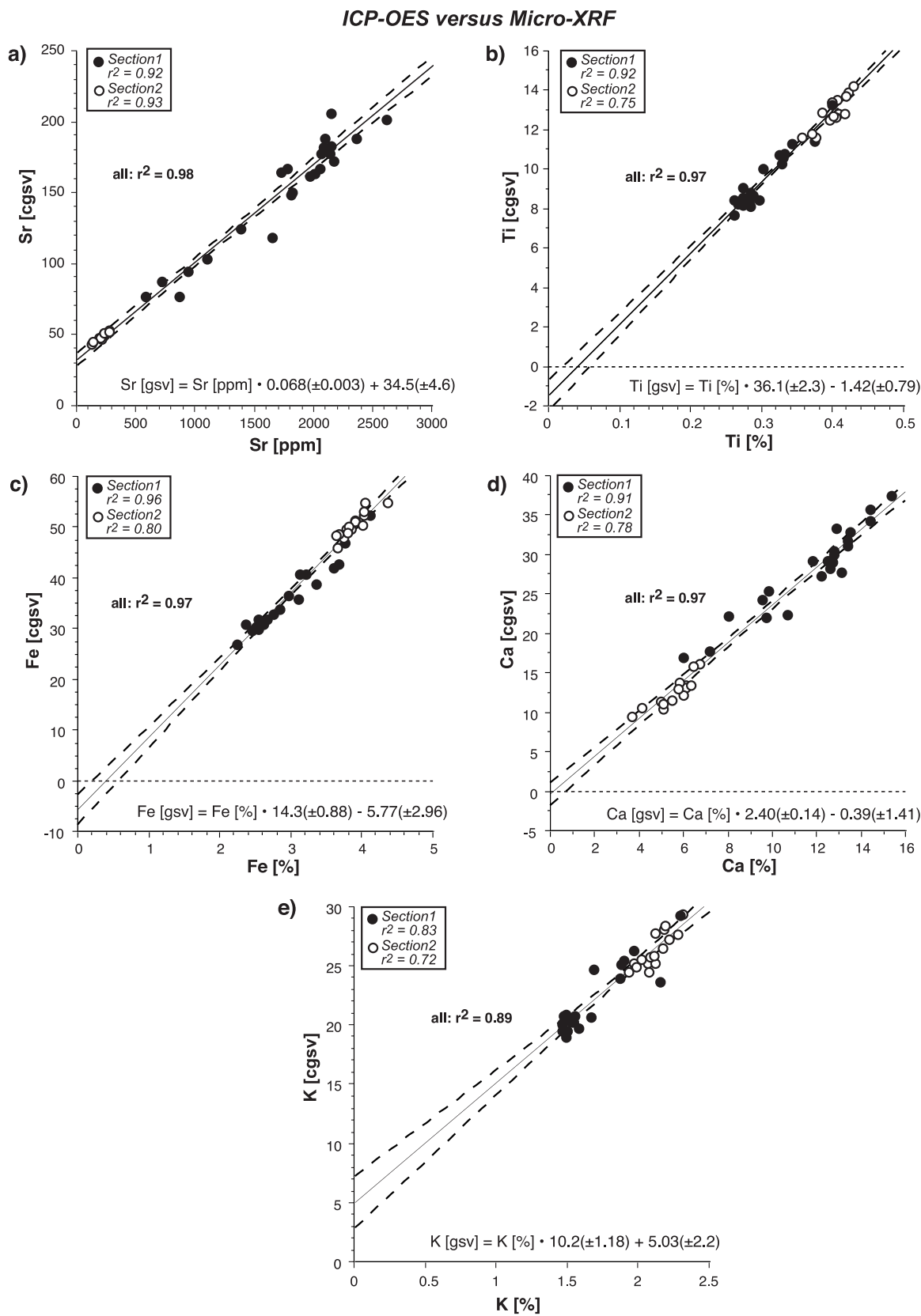
ICP-OES versus Micro-XRF

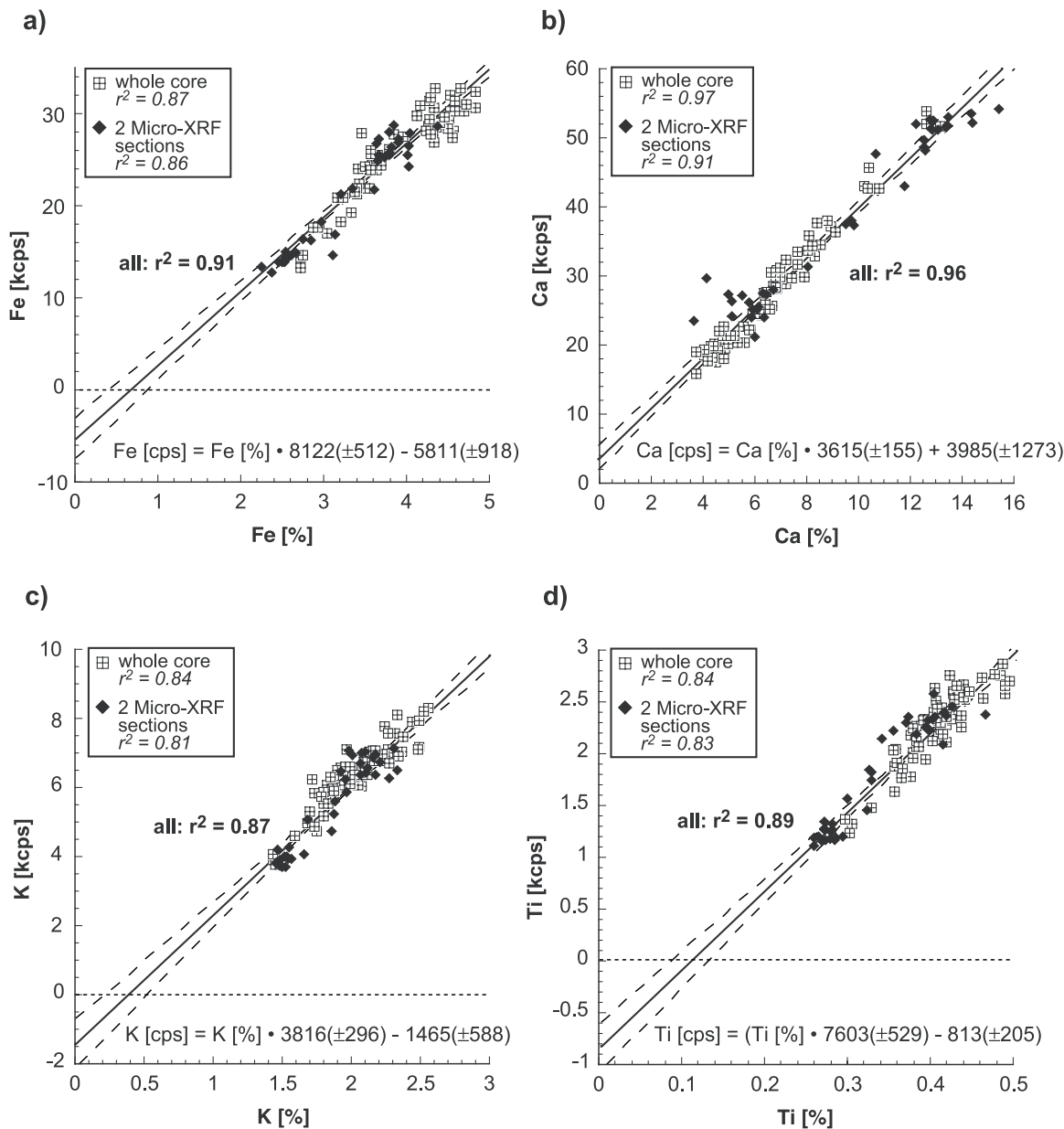a) Sr [cgsv] vs Sr [ppm]
Section1 r2 = 0.92
Section2 r2 = 0.93
all: r² = 0.98
Sr [gsv] = Sr [ppm] · 0.068(±0.003) + 34.5(±4.6)

b) Ti [cgsv] vs Ti [%]
Section1 r2 = 0.92
Section2 r2 = 0.75
all: r² = 0.97
Ti [gsv] = Ti [%] · 36.1(±2.3) - 1.42(±0.79)

c) Fe [cgsv] vs Fe [%]
Section1 r2 = 0.96
Section2 r2 = 0.80
all: r² = 0.97
Fe [gsv] = Fe [%] · 14.3(±0.88) - 5.77(±2.96)

d) Ca [cgsv] vs Ca [%]
Section1 r2 = 0.91
Section2 r2 = 0.78
all: r² = 0.97
Ca [gsv] = Ca [%] · 2.40(±0.14) - 0.39(±1.41)

e) K [cgsv] vs K [%]
Section1 r2 = 0.83
Section2 r2 = 0.72
all: r² = 0.89
K [gsv] = K [%] · 10.2(±1.18) + 5.03(±2.2)

Figure 5

Figure 6. Scatterplots for (a) Fe, (b) Ca, (c) K, and (d) Ti obtained from XRF-S (in kilo counts per second, kcps) and ICP-OES (in %). Windows show samples taken for ICP-OES distributed over the entire core, while black diamonds indicate samples originally taken for the calibration of Micro-XRF data. Dashed lines indicate the 95% confidence interval; dotted lines indicate the zero on the y axis. The regression equations are given in each graph, with corresponding deviations for the gradient and intercept. See also Tables 2 and 3 and text for further details.

in section 3.1, it is possible that increasing Ca intensities lead to absorption effects that influence the detection of Fe and Ti. The slightly positive intercept for Ca is solely due to the stronger data scatter seen in the second Micro-XRF data set. Indeed, the intercept value calculated with the first data set over the whole core (crossed squares in Figure 6b) is 1046 ± 1268, i.e., not significantly different from zero. The slightly negative intercept for K (Figure 6c) is also only caused by a stronger data scatter seen in the second Micro-XRF data set. The intercept value calculated with the first data set is -304 ± 732, i.e., also not significantly different
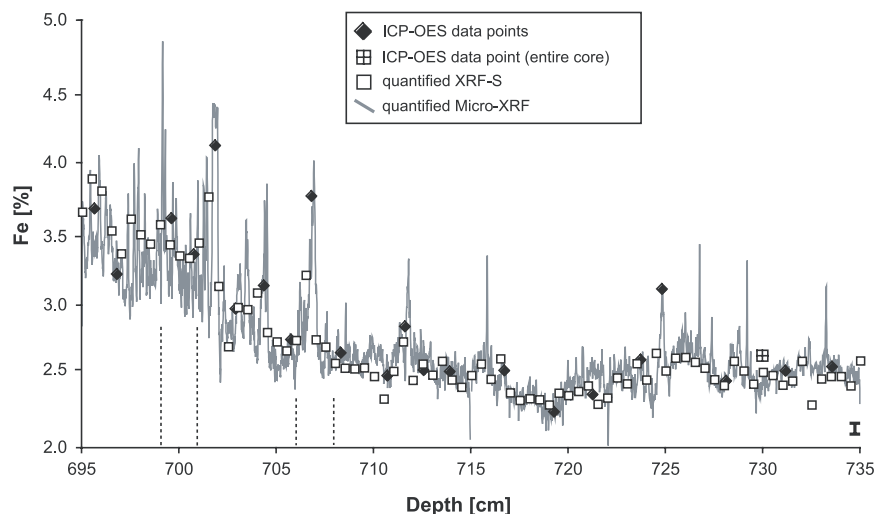
Figure 7. Fe (in %) versus depth for *Section 1* as a representative example for the comparison of Micro-XRF, XRF-S, and ICP-OES. The deviation of Micro-XRF and XRF-S data (average 3%, 1σ) data is indicated by the error bar (lower right). Dashed lines indicate the segments shown in Figure 8.

from zero. For Ti and Fe, the negative intercepts of both data sets show no significant difference.

3.3. Chemical and Structural Details of Micro-XRF and XRF-S

[30] After calibrating the two XRF-S and Micro-XRF data sets, we were able to study in detail the geochemical structure of the sediment core. To see whether the two XRF-S and Micro-XRF data sets match each other as well as the ICP-OES data, we present in Figure 7 a representative example of Fe data plotted versus depth for *Section 1*. We can see that the profiles obtained by Micro-XRF, XRF-S and ICP-OES plot very close to each other. Even for fine details, the individual XRF-S data points match the Micro-XRF data line very precisely. The discrepancy between Micro-XRF and XRF-S data is generally low ($\leq$3% relative, 1σ), demonstrating (1) the overall high technical accuracy and (2) that both non-zero y axis intercepts for the correlation of Micro-XRF and XRF-S Fe (Figures 5c and 6a) have no significant influence on the data quantification.

[31] As mentioned above, one of the major advantages of Micro-XRF is the production of highly detailed element maps. In Figures 8a and 8b, we present two examples (of segments) taken from *Section 1* showing all element maps as well as a preliminary element map for sulfur (for which measurement parameters still need calibration). Figure 8a depicts finely laminated sediments, while Figure 8b shows a thick irregularly shaped lamina

within a rather homogenous sequence. Light colors correspond to high element contents and dark colors correspond to low element contents. To a first approximation, the contents of Fe, Ti and K decrease while the contents of Ca and Sr increase with depth. Lamination in Figure 8a, for example, is clearly picked out by Fe, Ca and Sr, and, to a somewhat lesser extent, by Ti and K. The thick lamina is rich in Fe, Ti and K but low in Ca and Sr. The very light structures in the sulfur and iron maps indicate the presence of sulfides (usually pyrite). Individual foraminifera tests can be traced by sharp round structures that yield, for example, high Ca, low Sr and approximately zero Fe contents. Distinctly visible minute spots rich in Ti are most likely due to the presence of heavy minerals (e.g., rutile or ilmenite).

[32] Besides sediment input changes, an element profile can also be shaped by dilution by $CaCO_3$. A usual way to circumvent the problem is to calculate element profiles on a carbonate free basis. The Ca profile can be used to generate a $CaCO_3$ profile after crosschecking with other techniques based on measuring CO_3. Alternatively, it is possible to consider element ratios. We calculated the Fe/Ti ratio to see whether $CaCO_3$ dilution is a significant problem in the described section. As seen in Figure 8 the variations in Fe are mostly supported by the Fe/Ti ratio, which indicates that $CaCO_3$ dilution is not a major effect. In addition, peaks in the Fe/Ti ratio could be either due to changes in background material (i.e., provenance) or due to diagenetically (in situ) formed phases
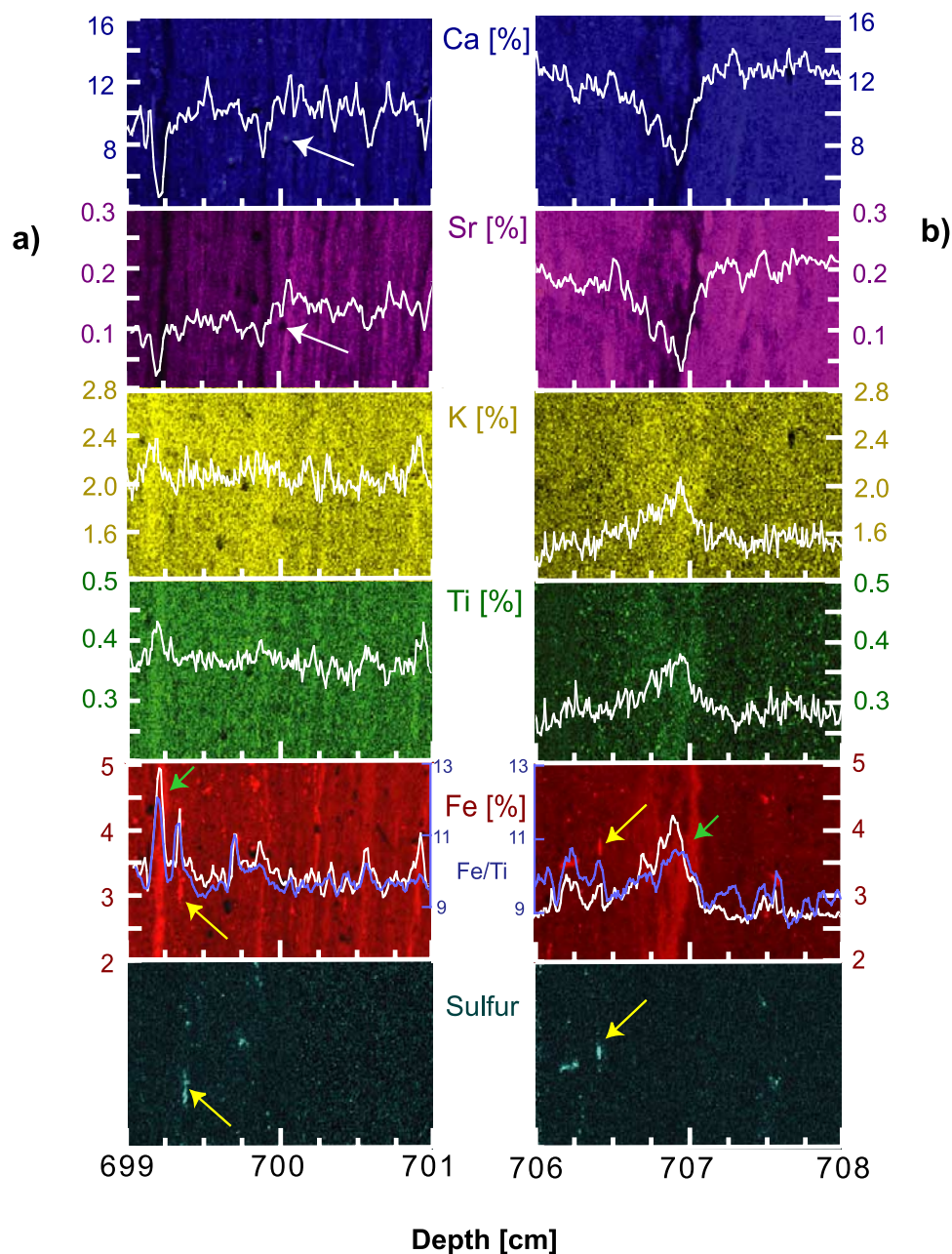
Figure 8. (a and b) Two segments from *Section 1* showing element maps and their corresponding profiles as well as a preliminary map for sulfur contents versus sediment depth. White arrows indicate an individual foraminiferal test (high in Ca, low in Sr). The presence of diagenetical Fe-sulfides (most likely pyrite) causing peaks in Fe and Fe/Ti is shown by the yellow arrows. The green arrows indicate peaks in Fe and Fe/Ti, which are most likely due to provenance changes. Note also the dispersal of minute Ti-rich phases as indicated in Figure 8b.

such as pyrite. By means of the sulfur maps one can distinguish whether the Fe/Ti signal is related to provenance or diagenetical changes. For example, the highest Fe/Ti peak in Figure 8a is caused by provenance changes, whereas the highest Fe/Ti peak in Figure 8b is due to diagenetical pyrite. This is a clear illustration of the usefulness of both element maps and profiles, leading to unambiguous interpretations.

4. Conclusions and Outlook

[33] With this study, we illustrate the accuracy and usefulness of a recently developed Micro-XRF

technique applied to paleo-geochemical research. We present data for Ca, Fe, K, Sr, Ti and S, which were obtained by a Micro-XRF analyzer (Micro-XRF) with 100-μm resolution and by an XRF whole-core scanner (XRF-S) with 5-mm resolution for selected wet sediment sections from a continental margin sediment core. The Micro-XRF technique produces highly resolved two-dimensional element maps. On the basis of overlap measurements of successive maps, we were able to calculate individual element profiles. We successfully quantified the two XRF data sets using discrete subsamples analyzed by ICP-OES. In this context, we discuss the advantages and limitations of both XRF techniques. A comparison of the two XRF data sets (e.g., using Fe) on a 5-mm resolution demonstrates the overall high consistency and accuracy of all the techniques used. Nevertheless, making use of XRF maps for K and Ti may be difficult for some sediments with high carbonate content, which leads to low K and Ti concentrations and thus reduced precision. Apart from these reservations, the capability to measure elements with a highly focused 100 to 10-μm X-ray beam allows the elemental analysis of single spots, grains or very small areas (such as pyrite, foraminifera tests, Ti-minerals etc.). Overall, element profiles and detailed element maps clearly show that Micro-XRF is a powerful tool for tracing the extent and timing of chemical, mineralogical and sedimentological transitions. Combining Fe/Ti profile and sulfur maps allows discriminating between provenance and diagenetical effects on the Fe profile, which is often a crucial issue in geochemical studies. This example highlights the usefulness of the XRF maps and clearly distinguishes the Micro-XRF from other technical devices producing elemental profiles only. Since Fe (and other redox-sensitive metals) are typically enriched close to diagenetical fronts, as best seen in turbidites and sapropels, the Micro-XRF is thus a very promising tool for analyzing metal contents in such sediments.

Acknowledgments

References

Haug, G. H., D. Günther, L. C. Peterson, D. M. Sigman, K. A. Hughen, and B. Aeschlimann (2003), Climate and the collapse of Maya civilization, *Science*, *299*(5613), 1731–1735.

Heinrichs, H., and A. G. Herrmann (1990), *Praktikum der Analytischen Geochemie*, Springer, New York.

Hosokawa, Y., S. Ozawa, H. Nakasawa, and T. Nakayama (1997), An X-ray guide tube and a desk-top scanning X-ray analytical microscope, *X-Ray Spectrom.*, *26*, 380–387.

Jansen, J. H. F., S. J. Van der Gaast, B. Koster, and A. J. Vaars (1998), CORTEX, a shipboard XRF-scanner for element analyses in split sediment cores, *Mar. Geol.*, *151*(1–4), 143–153.

Kido, Y., T. Koshikawa, and R. Tada (2006), Rapid and quantitative major element analysis method for wet fine-grained sediments using an XRF microscanner, *Mar. Geol.*, *229*(3–4), 209–225, doi:10.1016/j.margeo.2006.03.002.

Koshikawa, T., Y. Kido, and R. Tada (2003), High-resolution rapid elemental analysis using an XRF microscanner, *J. Sediment. Res.*, *73*(5), 824–829.

Peterson, L. C., G. H. Haug, K. A. Hughen, and U. Röhl (2000), Rapid changes in the hydrologic cycle of the tropical Atlantic during the last glacial, *Science*, *290*(5498), 1947–1951.

Röhl, U., and L. J. Abrams (2000), High resolution, downhole, and non-destructive core measurements from sites 999 and 1001 in the Caribbean Sea: application to the Late Paleocene Thermal Maximum, *Proc. Ocean Drill. Program Sci. Results*, *165*, 191–204.

Rose, J., et al. (2006), Applications of a 10 μm spot size laboratory Micro-XRF to environmental sciences, paper presented at EXRS European Conference on X-Ray Spectrometry, CEA-LIST-LNHB, Paris, 19 –23 June .

Schnetger, B., H. J. Brumsack, H. Schale, J. Hinrichs, and L. Dittert (2000), Geochemical characteristics of deep-sea sediments from the Arabian Sea: A high-resolution study, *Deep Sea Res., Part II*, *47*, 2735–2768.

Tertian, R., and F. Claisse (1982), *Principles of Quantitative X-Ray Fluorescence Analysis*, 319 pp., Heyden, London.

von Rad, U., A. Khan, W. H. Berger, D. Rammlmaier, and U. Treppke (2002), Varves, turbidites and cycles in upper Holocene sediments (Makran slope, northern Arabian Sea), in *The Tectonic and Climatic Evolution of the Arabian Sea Region*, edited by P. D. Clift et al., *Geol. Soc. Spec. Publ.*, *195*, 387–406.